Ultra-thin AAO membrane as a generic template for sub-100 nm nanostructure fabrication

Hossein Robatjazi [†,††,‖,⊥], Shah Mohammad Bahauddin [†,††,‖,⊥], Luke H. Macfarlan [#]; Sidan Fu [#];

Isabell Thomann *[,†,††,‡,§,‖,⊥]

[†]Department of Electrical and Computer Engineering, [‡]Department of Materials Science and NanoEngineering, [§]Department of Chemistry, [‖]Laboratory for Nanophotonics, [⊥]Rice Quantum Institute (RQI), [#] REU RQI program, [††]Rice Center for Quantum Materials, Rice University, 6100 Main Street, Houston, Texas 77005, United States.

Corresponding Author

* Email: isabell.thomann@rice.edu

Abstract

Anodic aluminum oxide (AAO) templates are emerging as a platform for simple, cost-effective, high-throughput top-down nanofabrication of regular arrays of nanostructures. Thus far, however, AAO pattern transfer has largely been restricted to smooth and chemically inert surfaces, mostly Silicon substrates. Here, we present a more generalizable strategy for preparing free-standing through-hole ultrathin alumina membranes (UTAMs) and transferring them to both smooth and rough substrates, thereby enabling the fabrication of centimeter-scale arrays of nanostructures with sub-100 nm feature diameters on almost arbitrary substrates. To validate the utility of our procedures, we transferred UTAMs to surfaces relevant for photocatalytic applications and prepared plasmonic photocathodes consisting of dense arrays of size-controlled sub-100 nm Au and Ni nanodots on top of chemically non-inert NiO_x thin films. To demonstrate the functionality of the fabricated structures, we used a plasmonic photocathode consisting of an array of sub-50 nm Au nanodots on NiO_x/Al substrates to drive direct, plasmon-enhanced photoelectrocatalysis and found excellent device performance. We also successfully decorated very rough fluorine-doped tin oxide substrates with an array of high-density sub-100 nm nanodots. Our results extend the opportunities for AAO masks to serve as generic templates for novel applications that were previously prohibited by lack of methods to transfer to the required substrate.

Introduction

Since the pioneering works by Masuda et al. [1] [2], anodic aluminum oxide (AAO) templates with their regular hexagonal array of monodisperse pores have become well-adopted for simple and cost-effective, yet high-throughput top-down nanofabrication [3-15]. The thickness, periodicity and diameters of the pores of these alumina templates are easily controlled and pores can be employed for material deposition or removal. The resulting one-dimensional nanostructure arrays have been assembled to create complex architectures with a wide range of applications in plasmonics and metamaterials [16,17], chemical separation [18,19], solar energy conversion and energy storage [20-22], catalysis [21-25], and sensing [9,26]. In most if not all applications, the substrate to which the nanopattern is transferred plays a critical role since it influences the optical, binding, electronic[27] and catalytic properties. Thus far, however, AAO pattern transfer was restricted to smooth and chemically inert surfaces, mostly silicon substrates.

AAO templates are most commonly employed for electrochemical deposition [7] [28] [29] [30] and physical vapor deposition [31] of one-dimensional structures in high aspect ratio channels with large pore sizes. In contrast, applications of AAO- membrane assisted nanostructure fabrication with sub-100 nm particle diameters have been limited, because fabrication requires the preparation of ultrathin alumina membranes (UTAM) with an aspect ratio (pore length to pore diameter) of less than 6:1 to avoid a shadowing effect [6]. Some of the challenges in preparing and transferring these delicate UTAMs, and subsequent efficient material deposition through the membrane have recently been addressed by Meng [8] and Al Haddad [32]. Meng [8] demonstrated the large-scale fabrication of ultrathin free-standing AAO membranes and intact transfer to Si substrates with subsequent sub-100 nm nanopattern fabrication. However, ion milling to remove the barrier layer is expensive and can adversely affect the underlying substrate. In the work by Al Haddad [32] the

base Al layer and barrier layer were removed by wet chemical etching after intact transfer of the UTAM to the Si substrate. Although wet chemical etching with a $CuCl_2$/HCl solution mixture works well for chemically inert Si substrates, this technique is not practical for other applications. PMMA (polymethylmethacrylate) is commonly used as a thin supportive layer on the UTAM. However, organic residues that are left from dissolving the polymeric layer are a potential source of surface contamination. Furthermore, this approach is not applicable to substrates that are not chemically compatible with the organic solvents used for removal of the organic supportive layer. Therefore, nanofabrication of structures with sub-100 nm features has been largely restricted to Si substrates [2 6 33 34 35 36 14 37] because of their chemical compatibility. The smooth surface of Silicon wafers also provides an excellent contact area with the AAO membrane, which is retained either via Van der Waals interactions or through surface treatment on the Si surface [8]. Challenges become even more formidable when attempting to transfer these fragile UTAM masks to rough substrates.

Here, we present a strategy for preparing free-standing through-hole ultrathin alumina membranes (UTAMs) suitable for the fabrication of nanostructures with sub-100 nm diameter on a wide range of substrates and specifically demonstrate their transfer to both smooth and rough substrates relevant for photocatalytic applications. This fabrication strategy enabled us to prepare centimeter-scale plasmonic photocathodes consisting of dense arrays of size-controlled sub-100 nm Au and Ni nanodots on top of NiO_x thin films, which could not have been fabricated with standard AAO transfer techniques since the substrate is degraded when the commonly used organic solvents are applied. Specifically, we fabricated a plasmonic photocathode consisting of an array of sub-50 nm Au nanodots on NiO_x/Al substrates that achieved large photocurrents when driving direct plasmon-enhanced photoelectrocatalysis. We also successfully decorated very rough substrates of fluorine-doped tin oxide (FTO, 200 nm peak-to-peak, and 33 nm RMS surface

roughness) coatings with an array of high-density sub-100 nm nanodots. These results extend the opportunities for AAO masks to serve as generic templates for novel applications that were previously prohibited by lack of methods to transfer to the required substrate.

Figures 1a-f are graphical illustrations of the fabrication of a highly ordered array of nanodots. The steps for preparing a high-quality free-standing through-hole UTAM floating on water and subsequent transfer to the substrate of interest for material deposition are depicted. We prepared UTAMs with highly regular arrays of pores, with an initial average pore size of 37 nm and an interspacing distance of approximately 100 nm (Fig. 1g) via a two-step anodization of high-purity aluminum foil (99.999%) in 0.3M oxalic acid [2 38] (see Supporting Information). Before etching the base aluminum (Al) layer, a thin layer of polystyrene (2 wt% PS/$CHCl_3$) was coated on a centimeter scale alumina surface either through spin coating at 3000 rpm or simple drop casting. To facilitate dissolution of copper precipitation on the UTAM, the remainder of the base aluminum layer was detached in a solution of $CuCl_2$/HCl (3.4 gr $CuCl_2.2H_2O$, 50 mL 38% HCl, 100 mL Millipore water) at room temperature with a very low quantity of TX-100 additive (~ 50 μL initial value) to reduce surface tension [39] and a small quantity of HNO_3 (83%) additive (~ 2 mL initial value) in approx. 100 mL etching solution. During the etching process and afterward the UTAM was handled using a Nylon plastic strainer [40]. The removal of the barrier layer and the pore-opening process was carried out using 5% H_3PO_4 at room temperature for different durations to obtain through-hole UTAMs with different pore diameters. Then, the UTAM was rinsed with deionized water and was left on the strainer for drying. After etching the base aluminum layer, a few large-sized Al residues remained at the bottom of the AAO membrane that made the subsequent material deposition process less efficient in particular on rough substrates. To solve this issue, we flipped the UTAM, before removing the polymeric layer, such that the face with the

smoother surface from electropolishing in the first step is placed on the substrate. Next, we removed the PS layer by gently dropping a few ml of chloroform on the AAO/polymer film supported by the strainer. This step was followed by immersion of the entire UTAM in chloroform for about 10 minutes to remove any organic residues. After the solvent has evaporated, the strainer was gently pushed against the water, such that surface tension pushed the UTAM upwards, and the membrane detached from the strainer and started floating on water (Figure 1c,h). The floating UTAM was transferred to the substrate of interest (Figure 1d,i) without any surface treatment. We dried the sample at room temperature in a tilted position such that water could slowly run off the sample, and the membrane was stretched and perfectly adhered to the substrate. Alternatively, the through-hole UTAM was supported by a retained Al frame at the edges of the UTAM (Supporting Information S4). Here the polymer layer was completely removed by vertical immersion of the sample in $CHCl_3$ after barrier layer removal in H_3PO_4. A similar approach was previously employed for transferring large-scale UTAMs to surface treated Si substrates [8]. However, this approach required ion milling for barrier layer removal and membrane thinning and can damage the underlying substrate, such as the NiO_x thin films studied here. We also found that the transfer of the UTAM to the substrate was more efficient when the transfer was carried out in water because of the stronger adhesion that is essential for its application as an evaporation mask. The applied polymer coating does not only impede breaking or ripping of the UTAM during the etching process in the erosive etching solution, but it also limits H_3PO_4 to only etch the bottom surface of the barrier layer that is crucial for controlling the pore size [37]. Indeed, we also performed Al etching on unsupported UTAMs in saturated $CuCl_2$ solution followed by removing Al residuals in a mixture of $CuCl_2$ and HCl as highlighted in previous work [41]. However, in this procedure, the

centimeter scale free standing sub-300 nm thick AAO often broke, cracked, or sunk in the solution and pore opening was less controlled.

Figure 1i shows a digital image of the UTAM placed on top of a 40 nm thick NiO_x film prepared on a highly reflective Aluminum substrate (see Supporting Information). The scanning electron microscopy (SEM) images of the UTAM (Figure 2a) show that the membrane is approximately 220 nm thin. We utilized the UTAM as an evaporation mask for nanopatterning on top of a NiO_x film. Figure 2b shows a hexagonal array of Au nanodots on NiO_x obtained by evaporating 15 nm of Au through the UTAM. The particle diameters are centered around 50 nm (and range from 40 to 57 nm). The SEM images show that the dots do not have perfect spherical cross-sections. We attribute their broad particle size distribution and distortion of the shape of the particles to misalignments of the holes with the Au evaporation source that is more than 50 cm away from the sample in our e-beam evaporator. The deviation from the spherical shape could also be from the non-circularity of the pores at the bottom side of the membrane during barrier layer removal in H_3PO_4 [42]. By annealing the sample at 400°C for about 2hr in air we obtained particles with a circular cross-section, and the average particle diameter decreased by more than 10 nm to 36 nm with an overall narrower size distribution (± 4 nm) and an average inter-particle distance of approx. 64 nm (Figure 2c). The decrease in particle diameter was accompanied by an increase in particle height to 30 nm (Figure 2d). As visible in the low-magnified SEM images (Supporting Information S5, Fig. a-c) the nanodots are arranged in uniform intervals and with high density on the surface (ca. 1×10^{10} cm^{-2}) which is further supported by the homogenous greenish color of the sample (inset Fig. 2d). We furthermore controlled the size of the nanodots by controlling the pore size. Figure 3 shows highly-ordered arrays of nanodots with average diameters of ca. 48 nm, 64 nm, and 80 nm, and corresponding inter-particle distances of ca. 52 nm, 36 nm, and 20 nm

fabricated on 40 nm thin NiO_x films by evaporating 20 nm of Au through the UTAM. The large-area SEM images (Supporting Information S5, Fig. d-g) show decoration of the NiO_x surface with uniformly spaced nanodots with a narrow size distribution (± 5nm) even in regions where the NiO_x film has few hundred-nm high bumps. In addition to fabricating gold dots with diameters down to 36 nm, we also prepared interesting oligomers within the pores by evaporating a 5 nm thick Au film and subsequent annealing. We found single, dimer, trimer, quadrumer and pentamers of nanodots with sub-10 nm gaps and particles sizes from 5 to 30 nm within the pores (Supporting Information S5, Fig. h).

The developed procedure provides a generic AAO template that can be used for top-down nanofabrication on a large range of substrates and deposition of a broad variety of materials. To demonstrate these capabilities, we prepared nickel nanodots with sub-100 nm particle diameter on NiO_x (see SEM image Figure 4a). Recent work showed the importance of nanostructured metal oxides (NMOs) as a promising building block in the fabrication of biosensors [43]. Therefore, such Ni nanodots/NiO_x structures may open opportunities in plasmonic biosensor designs with improved sensing characteristics while offering remote control via external magnetic fields. Additionally, the plasmonic nickel nanoantennae are emerging as an attractive area of research owing to their distinct plasmonic features in conjunction with strong magnetic properties [44].

To demonstrate the versatility of our nanopatterning approach, we also transferred the nanodot pattern onto rough substrates of ~ 940 nm thick FTO (approx. 33 nm RMS, 200 nm peak-to- peak surface roughness) and ~150 nm thick ITO (approx. 0.8 nm RMS, 7 nm peak-to-peak surface roughness). Figure 4b shows a transparent appearing 120 nm thin UTAM transferred to the 940 nm thick clearly visible rough FTO. As mentioned above, we observed several micron-sized Al residues on the backside of the UTAM (Supporting Information S6) that impede efficient transfer

to the rough substrate. To circumvent this problem, we flipped the film before removing the polymer layer such that its smoother surface faced the substrate. Then 10 nm and 15 nm of Au were deposited on FTO and ITO, respectively. As can be seen in Figure 4 c,d both substrates were successfully patterned by dense arrays of hexagonally arranged sub-50 nm particles. While many works have previously reported nanopatterning on smooth substrates such as Si, to the best of our knowledge, transfer of sub-50 nm particle sizes to rough substrates has not been reported to date. Furthermore, fabrication procedures that preserve the quality of the underlying substrate are of paramount importance for the quality of devices. For example, when we carried out polymer removal from the AAO mask with the standard procedure employing a $CHCl_3$ solvent the underlying NiO_x layer was damaged significantly (Supporting Information S7). Also, we observed a significant decrease in the density of particles that we ascribed to micron-sized polymer residues left on the UTAM preventing material deposition through the channel.

Recent years have witnessed intense interest in implementing plasmonic and dielectric nanostructures for enhancing the efficiency of light-harvesting devices for photovoltaic [45-47] and photocatalysis applications [24,48-53]. Most recently, plasmonic hot-carrier generation via non-radiative surface plasmon decay has been exploited as a novel mechanism for solar-to-fuel conversion [23 54 55] that promises to open up novel photoreduction pathways that are inaccessible by conventional mechanisms such as the application of heat or an electrochemical bias. In this regard, we recently developed a novel Schottky junction-free plasmonic photoelectrode architecture, consisting of a dense layer of randomly dispersed gold nanoparticles with a broad size distribution for direct plasmon-driven photoelectrocatalysis of water through efficient hot-electron generation and injection into the adsorbed molecules [56]. This novel architecture achieved high efficiency of hot-carrier injection to adsorbed water molecules by i) avoiding the Schottky

barrier that is commonly used for preserving the energy of hot-electrons; ii) achieving increased light absorption using an architecture inspired by optical impedance matching concepts; [47 57] and iii) facilitating efficient charge carrier separation by a NiO-based selective hole transmitting layer [56 58].

Here, we validated the utility of our free-standing through-hole ultrathin alumina membranes (UTAMs) transfer procedures by demonstrating a functional device. We chose to fabricate plasmonic photoelectrodes from the same components Au/NiO_x/Al that had been employed in our previous publication[56] for several reasons: First, it is a very interesting system in terms of hot-carrier generation in gold nanoparticles and selective carrier filtration by means of the underlying NiO_x layer. Second, it allows us to directly compare the photocurrent, absorbed fraction and plasmon frequency of a *highly ordered* nanoarray of monodisperse gold nanoparticles to those of dense, *randomly deposited* gold nanoparticles[56] as used in our previous publication[56]. Figure 5a illustrates the plasmonic photoelectrode architecture with the plasmonic nanodot array in direct contact with water. The NiO_x film below the Au dots has both, an electrical and an optical function: The electronic function of the NiO_x layer is to confine the generated hot electrons within the Au nanoparticles and to selectively block the electrons but transmit the holes to the aluminum back electrode. The optical function of the high-refractive index ($n \sim 2.3$) NiO_x is to serve as a highly transparent wide bandgap spacer layer between the plasmonic nanodots and the aluminum back reflector for maximum and broadband (~ 100 nm) light absorption within the single layer of nanoparticles. Although the components Au/NiO_x/Al used in our present and past work are the same, there is a significant difference between the geometry of gold (Au) nanoparticles (NPs) for the two devices: In our previous work[56] we employed a single layer of randomly deposited Au NPs with heterogeneous size distribution whereas in the present work we demonstrate a highly ordered

array of hemi-spherical NPs with monodisperse size distribution and a different fill fraction. The change in geometry results in different absorption spectra and position of the plasmon peak: For the randomly deposited highly anisotropic NPs with heterogeneous size distribution and higher fill factor, the absorbed fraction is higher and we obtained broad band absorption and a broader plasmon resonance centered around 800 nm[56] whereas for the highly ordered nanoarray with monodisperse Au NPs and lower fill fraction the plasmon resonance is centered around 650 nm and is less broad (Figure 5c).

The band energy schematic of the photoelectrode is depicted in Figure 5b. Light absorption within the Au particles results in the excitation of a surface plasmon resonance at 650 nm (1.9 eV) which can decay nonradiatively, resulting in hot-carrier generation. The plasmon-induced hot electrons adopt a Fermi-Dirac distribution, and in our case electrons in the high-energy tail of the distribution should have sufficient energy to overcome the thermodynamic and kinetic barrier to drive the hydrogen evolution reaction (the thermodynamic potential for the HER lies at ~1 eV above the Fermi energy of Au). Hot electrons can also be generated from direct photoexcitation of interband transitions. However, in our previous study [56], we measured the wavelength-resolved photocurrent and found that photocarriers excited from the interband transition are not energetic enough to drive the HER. The upper edge of the d-band is located at ~ 2.3 eV below the Fermi level of Au [59] and therefore under optical excitation with a wavelength of 400 nm (maximum energy of ~ 3.1 eV), near the edge of the solar spectrum, the electrons excited from the d-band are typically promoted to unoccupied states with a maximum of 0.8 eV above Fermi level, making them insufficiently energetic.

Figure 5c shows the measured total absorbed fraction in air versus the simulated absorbed fraction in Au in air and the simulated total absorbed fraction in air for the photocathode consisting

of Au nanodots with an average diameter of 36 nm and 30 nm thick, and 100 nm center-to-center particle distances on a 40 nm thin NiO_x layer (sample shown in Fig. 2d). As can be seen, the experimentally measured total absorption spectrum shows a plasmon resonance that matches qualitatively with the simulated absorption spectrum. In comparison with our previous study on randomly oriented anisotropic particles with heterogeneous size distribution and a broad plasmon resonance absorption, the plasmonic photocathode here exhibits a distinct plasmon resonance peak at 650 nm as the uniformly shaped nanodots possess uniform particle diameters arranged in an ordered array. The simulated absorbed fraction within the Au nanoparticles and the total absorbed fraction within the photoelectrode reaches about 85% and 95%, respectively at the plasmon resonance while the observed total absorption is about 50%. Further adjustment of the spacer layer thickness can result in absorption close to unity based on electromagnetic simulations. However, we decided to keep the NiO_x film 40 nm thin because of our well-established fabrication procedure and to maintain the electrical properties similar to our past work [56]. As expected, both the experimentally measured total absorption and the simulated absorbed fraction within the Au nanodots show increased absorption at wavelengths below 550 nm due to the interband transitions from the d-band.

Figure 5d shows a linear sweep voltammetry measurement of the plasmonic photocathode decorated with an array of Au nanodots with 36 nm (± 4 nm) diameter and 30 nm height (Fig. 2c,d) immersed in a nitrogen-purged solution of 0.5 M Na_2SO_4 buffered at pH 5.0 under chopped illumination at about one sun (100 mW/cm^2). Photoelectrochemical measurements were performed in a cell with a three-electrode configuration where Ag/AgCl (in sat. 3.0 M KCl) and a Pt mesh were used as reference and counter electrodes, respectively. The onset photocurrent at 0.4 V with respect to the RHE is approximately 0.35 $\mu A/cm^2$ and reaches up to 8.2 $\mu A/cm^2$ at 0V

versus the RHE. The control experiment for a NiO_x/Al sample without Au nanodots (red line in Fig. 5d) showed a photocurrent of about 0.25 $\mu A/cm^2$ at an electrode potential of 0V vs. RHE. Thus, the photocurrent in the presence of the Au nanodots array is ~35x larger. We previously performed additional control experiments on NiO_x/Al samples[56]: We optically characterized NiO_x and calculated a band gap of 3.45 eV with near zero absorption at wavelengths longer than 525 nm. In that work, we also performed wavelength-resolved photocurrent measurements for NiO_x/Al samples without Au nanodots and no photocurrent was observed at wavelengths longer than 500 nm. These observations verified the lack of significant defect or trap state densities in the NiO_x. We also note that gap-mode coupling that could enhance absorption in the NiO_x layer by near-field enhancement is limited because the gold nanodots are well separated. Moreover, Mott Schottky measurements on a sample without plasmonic nanoparticles showed that the NiO_x is p-type (hole concentration on order of $10^{18} cm^{-3}$) and has a flat band potential close to the Fermi level of gold[56]. This means that the valence band edge of NiO_x is favorable for hole transfer while charge transfer to a trap state near the conduction band (which is almost 3.4 eV away) cannot be driven by a plasmon resonance at 650 nm ($\approx$ 1.9 eV). Given the results of the control experiments, alongside with the absorption results of the plasmonic photocathode (Figure 5c), we propose that the photocurrent is due to direct hot-electron injection from the Au nanodots to adsorbed water molecules, in agreement with our earlier work [56] employing a random distribution of polydisperse gold particles on NiO_x/Al.

We note that the cyclic voltammogram of the plasmonic photocathode showed consistent photocurrents as a function of applied bias (Supporting Information S9). The observed photocurrents from this photoelectrode architecture based on a highly ordered array of hemi-spherical NPs with monodisperse size distribution and a relatively low fill fraction are on par with

recently demonstrated TiO_2-coated plasmonic gold Schottky junction geometries with large catalytic surface areas that also added platinum nanoparticles to catalyze the HER [23]. The absence of the degradation of photocurrents during repeated cyclic voltammetry and the large photocurrents demonstrate an excellent mechanical and electronic contact of the gold nanoparticles to the NiO_x/Al substrate (Supporting Information S9). The stability of the Au nanostructure itself should not be a matter of concern mainly because Au is well-known for its good stability in various device applications, including photocatalytic devices. In addition, AAO-based nanoarray fabrication is not limited to Au deposition and this is indeed one of the advantages of this technique. The quality of the interface between the nanodot array and the underlying substrate does not relate to the nature of the AAO-template based nanofabrication technique but instead mainly depends on the properties of the two materials and the deposition technique (e-beam evaporation, electrodeposition etc). For example, Au is known for its poor adhesion to silicon substrates when deposited by e-beam evaporation. To solve this problem, usually a titanium or chromium adhesion layer is deposited on the substrate before deposition of Au. Therefore, if needed, an adhesion layer can be deposited through the AAO pores prior to depositing the target material.

In our Au/NiOx device, we did not deposit any adhesion layer prior to Au deposition, mainly to avoid any contamination and to keep the interface simple for our study of carrier injection across the Au-NiOx interface. The large photocurrent density of 8.2 $\mu A/cm^2$ at 0V versus the RHE observed for our present, highly ordered array of hemi-spherical NPs with monodisperse size distribution but relatively low fill fraction compares favorably to our past results[56] on dense, randomly oriented anisotropic particles with heterogeneous size distribution.

Both, for our current work on highly ordered nanoarrays and our past work on random Au nanoparticles deposited on NiOx, the quality of Au/NiOx interface was excellent as highlighted by the large and stable photocurrents that we observed from our devices in comparison with the best published results for hot-electron generation and utilization[23,56].

In summary, we presented a protocol for nanopatterning of arrays with sub-100 nm features that overcomes past substrate limitations. Following our new protocol, plasmonic arrays consisting of sub-100 nm nanodots were fabricated on different substrates with different physicochemical surface properties, including chemically sensitive NiO_x thin films, and very rough FTO and ITO substrates. The performance of a plasmonic photocathode consisting of sub-50 nm nanodots array for plasmon mediated hot-electron injection from a Schottky junction-free device to water molecules for solar-to-chemical energy conversion was tested, and compares favorably with the best-published results [23] [56]. This work can provide the impetus for AAO-based fabrication of novel arrays of metallic and dielectric materials on generic substrates with applications in photovoltaics, photocatalysis, nanophotonics, and sensing.

Supporting Information Available: Details of the fabrication process, the spectrum of the light source, SEM images of the as-fabricated UTAM, SEM images of the free-standig UTAM, SEM images of nanodot arrays, electromagnetic simulation parameters, cyclic voltammetry measurements of plasmonic photocathodes. This material is available free of charge via the Internet at http://pubs.acs.org.

ACKNOWLEDGMENT We gratefully acknowledge support from the Robert A. Welch Foundation (Grant No. C-1825) and the National Science Foundation (NSF CAREER Award, CHE- 1352579). We thank John Haug for contributing the schematic in Figure 1.

Notes

The authors declare no competing financial interest.

Figure 1.

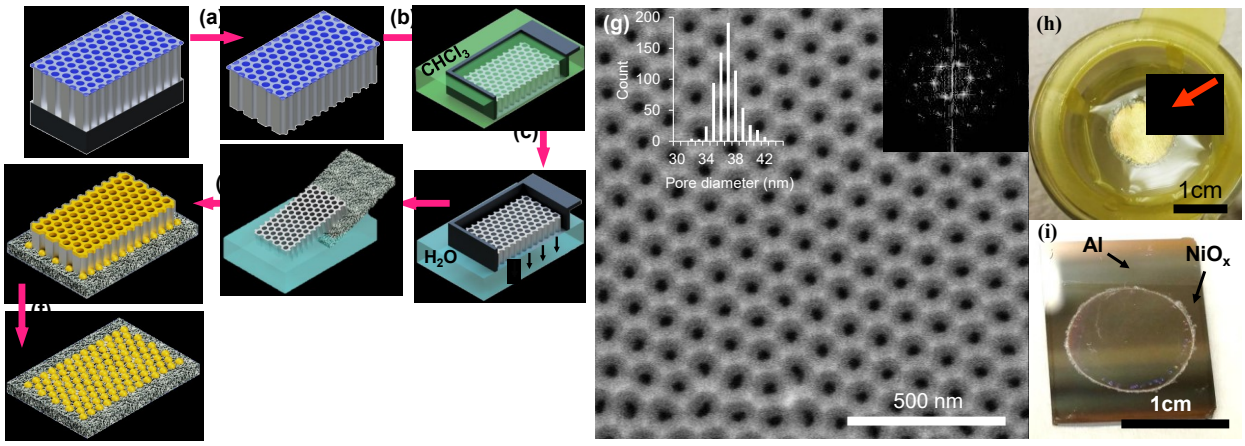

Figure 1. Schematic diagram illustrating the preparation process of a free-standing UTAM and subsequent transfer to a substrate of interest for nanostructure patterning (a-f). a) Etching of the underlying Al layer and pore opening b) Removal of the polystyrene layer in chloroform c) Floating of the UTAM on water d) Transfer of the UTAM to the substrate of interest e) Deposition of material through the nanopores f) Removal of the UTAM. g) SEM image of the as-fabricated UTAM on Al. The initial average pore size is about 37 nm with a periodicity of approx. 100 nm. The FFT results (inset) confirm a near-perfect hexagonal arrangement of the pores. h) Digital image of a free-standing UTAM with a thickness of less than 250 nm floating on water. i) Transfer of the UTAM to almost arbitrary substrates such as rough FTO or chemically non-inert 40 nm NiO_x thin films prepared on Al/Si (shown here).

Figure 2.

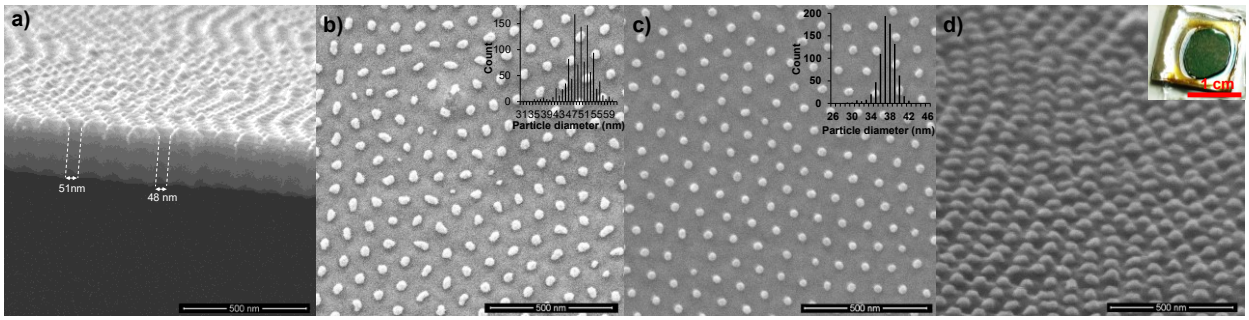

Figure 2. Fabrication of a highly-ordered, high-density Au nanodot array on NiO_x with uniform particle geometry. a) Cross-sectional SEM image of an UTAM with a thickness of less than 250 nm placed on a 40 nm thick NiO_x layer. b) NiO_x surface patterned with highly-ordered Au nanodot array with particle diameters around 49 nm by evaporating 15 nm of Au through a UTAM. c) Controlling the uniformity of the size of the Au nanodots by annealing the sample for approx. two hours at 400° C in air. After annealing, the Au nanodots adopted a hemispherical shape accompanied by a more than 10 nm decrease in particle diameter. d) Oblique-view of the sample after annealing shows Au nanodots with an average height of 30 nm. Inset: digital image of a photoelectrode consisting of a Au nanodot array on top of NiO_x/Al.

Figure 3.

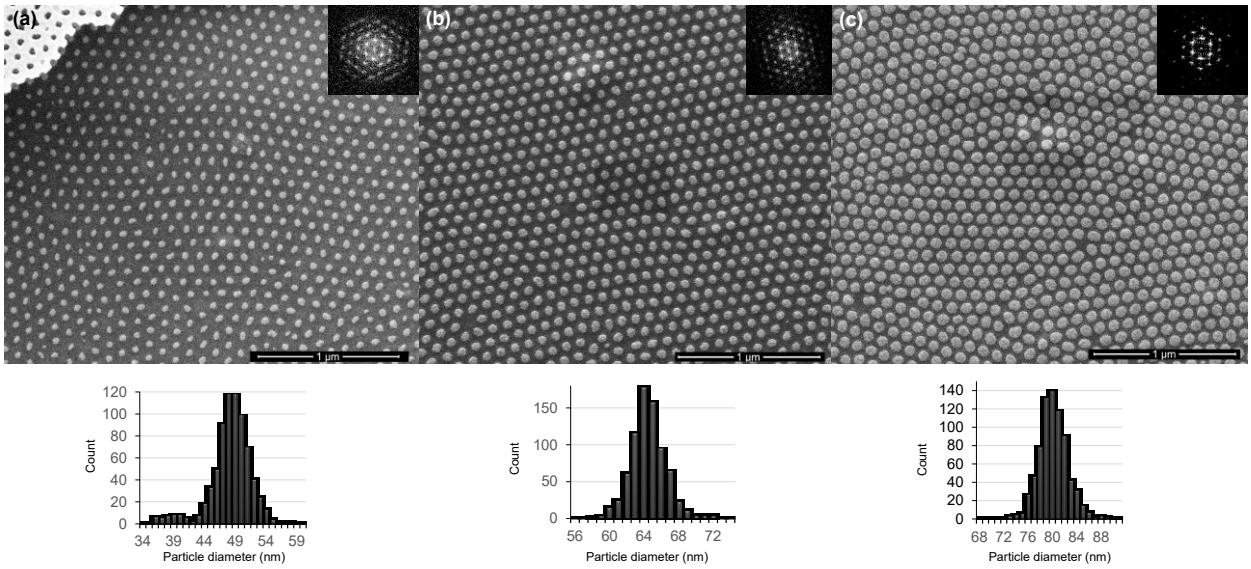

Figure 3. Fabrication of highly-ordered Au nanodot arrays on a NiO_x surface with tunable sub-100 nm particle diameters. From a) to c) the particle diameter is approx. 48 nm, 64 nm, and 80 nm, respectively. For all samples, the particle height and periodicity were 20 nm and 100 nm, respectively.

Figure 4.

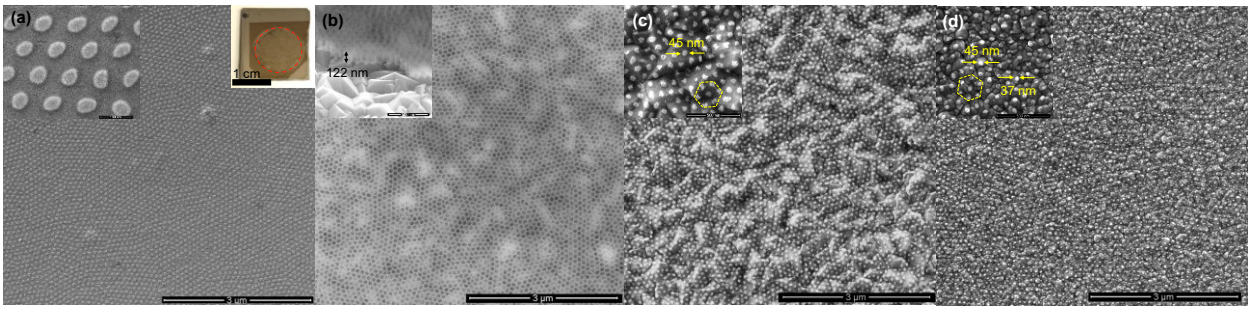

Figure 4. The UTAM serves as a generic deposition mask for metals and dielectrics that can be transferred to rough (FTO) and smooth (ITO) substrates, and also to chemically non-inert (NiO_x) substrates. None of these substrates required deposition of an adhesion layer. a) Fabrication of a sub-100 nm nickel nanodot array on a 40 nm NiO_x/Al/Si substrate by evaporating 20 nm of nickel through the UTAM mask. b) Plain-view and oblique-view SEM image of a UTAM mask (123 nm thick) successfully transferred to a very rough substrate of ~ 940 nm thick FTO (33 nm RMS, ~200 nm peak-to-peak surface roughness) for subsequent fabrication of nanodot arrays. c), d) Dense Au nanodot arrays with sub-50 nm particle size fabricated by evaporating 10 nm Au through the UTAM mask onto a rough FTO substrate (c) and 15 nm Au through the UTAM mask onto an ITO substrate (d) (0.8 nm RMS, 7 nm peak-to-peak roughness).

Figure 5.

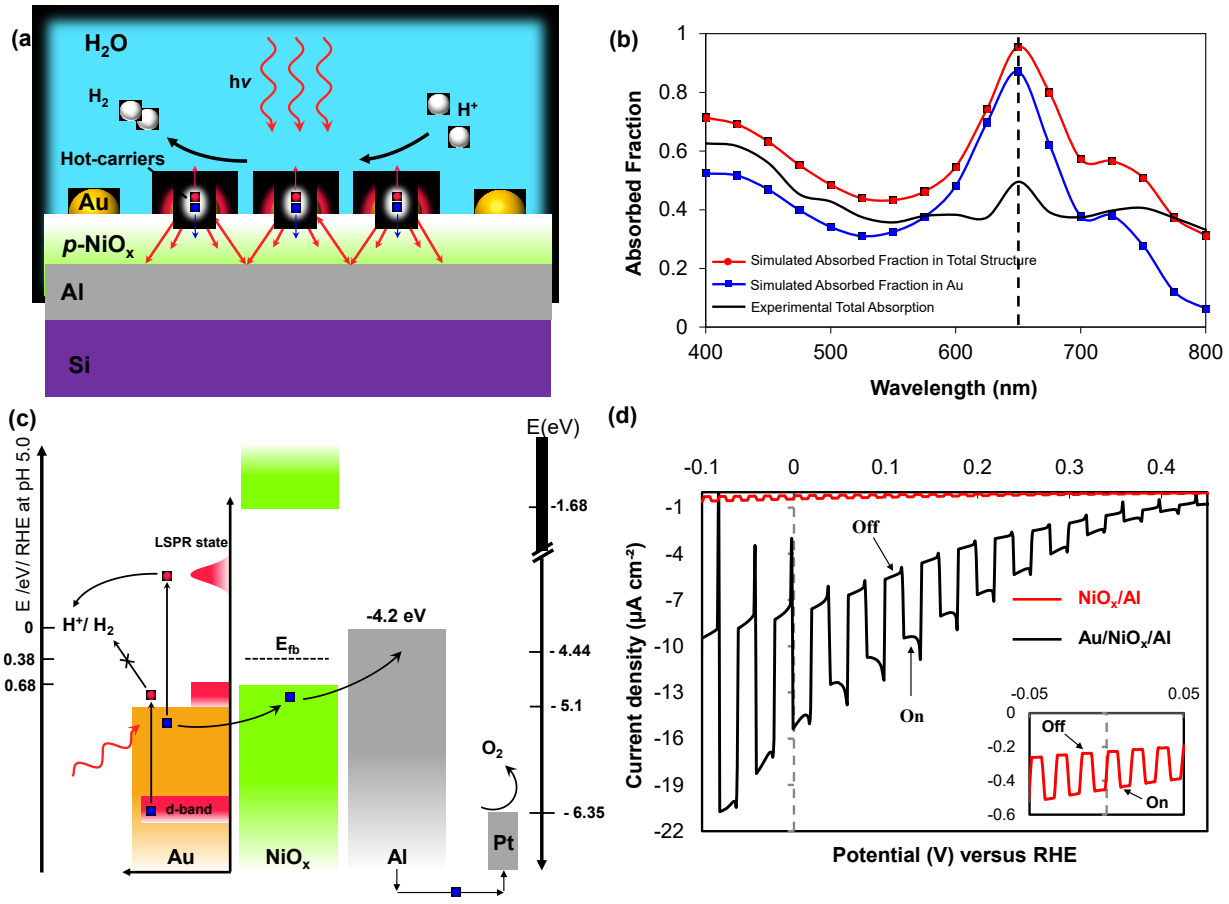

Figure 5. Photoelectrode architecture, operating principle, absorbed fraction and photoelectrochemical performance of a Schottky junction-free plasmonic photocathode. a) Solar-to-chemical energy conversion is driven by hot-carriers generated in a plasmonic photocathode consisting of an ordered array of Au nanodots, p-NiO_x as a selective hole transfer layer/electron blocking layer and an aluminum layer that serves simultaneously as a reflector and back electrode. Plasmon-induced hot electrons are directly injected from Au nanodots into the adsorbed molecular species, here into the water layer. b) Energy band schematic of the plasmonic photocathode. The nonradiative decay of the surface plasmon into hot electrons results in direct injection into water molecules to drive the hydrogen evolution reaction (HER) while hot electrons generated from interband absorption are not energetic enough to drive HER. The favorable band edges of

the NiO_x layer block electron transport while allowing for hole transport to the platinum counter electrode. c) Measured absorbed fraction in the photoelectrode in air as a function of wavelength, and simulated absorbed fraction in Au and simulated total absorbed fraction in the photoelectrode in air. The photoelectrode consisted of 30 nm thick Au nanodots with a diameter of 36 nm and a 100 nm center-to-center particle distance deposited on a 40 nm thick NiO_x layer on top of a 200 nm thick Aluminum layer. The measured plasmon resonance at 650 nm is in excellent agreement with the simulation results. d) The photoelectrocatalytic performance of the plasmonic photocathode (black) along with a control sample without Au nanodots (red) measured under total white light illumination (~ 100 mW cm^{-2}, AM1.5G filter) in a nitrogen-purged, 0.5M Na_2SO_4 electrolyte buffered at pH 5.0. The photocurrent was measured in a three-electrode photoelectrochemical cell configuration with a Pt mesh as the counter electrode and is plotted versus the reversible hydrogen electrode (RHE).

References

(1) Masuda, H.; Fukuda, K. Ordered Metal Nanohole Arrays Made by a Two-Step Replication of Honeycomb Structures of Anodic Alumina. *Science* **1995**, *268*, 1466-1468.

(2) Hideki, M.; Masahiro, S. Fabrication of Gold Nanodot Array Using Anodic Porous Alumina as an Evaporation Mask. *Jpn. J. Appl. Phys.* **1996**, *35*, L126-L129.

(3) Wu, Y.; Cheng, G.; Katsov, K.; Sides, S. W.; Wang, J.; Tang, J.; Fredrickson, G. H.; Moskovits, M.; Stucky, G. D. Composite mesostructures by nano-confinement. *Nat. Mater.* **2004**, *3*, 816-822.

(4) Li, J.; Sattayasamitsathit, S.; Dong, R.; Gao, W.; Tam, R.; Feng, X.; Ai, S.; Wang, J. Template electrosynthesis of tailored-made helical nanoswimmers. *Nanoscale* **2014**, *6*, 9415-9420.

(5) Zhang, A.; Hou, K.; Gu, L.; Dai, C.; Liu, M.; Song, C.; Guo, X. Synthesis of Silica Nanotubes with Orientation Controlled Mesopores in Porous Membranes via Interfacial Growth. *Chem. Mater.* **2012**, *24*, 1005-1010.

(6) Lei, Y.; Cai, W.; Wilde, G. Highly ordered nanostructures with tunable size, shape and properties: A new way to surface nano-patterning using ultra-thin alumina masks. *Prog. Mater. Sci.* **2007**, *52*, 465-539.

(7) Banholzer, M. J.; Qin, L.; Millstone, J. E.; Osberg, K. D.; Mirkin, C. A. On-wire lithography: synthesis, encoding and biological applications. *Nat. Protoc.* **2009**, *4*, 838-848.

(8) Meng, G.; Yanagida, T.; Nagashima, K.; Yanagishita, T.; Kanai, M.; Oka, K.; Klamchuen, A.; Rahong, S.; Horprathum, M.; Xu, B.; Zhuge, F.; He, Y.; Masuda, H.; Kawai, T. Facile and scalable patterning of sublithographic scale uniform nanowires by ultra-thin AAO free-standing membrane. *RSC Adv.* **2012**, *2*, 10618-10623.

(9) Lee, W.; Park, S.-J. Porous Anodic Aluminum Oxide: Anodization and Templated Synthesis of Functional Nanostructures. *Chem. Rev.* **2014**, *114*, 7487-7556.

(10) Cho, Y., Lee, W., Jhon, Y. K., Genzer, J. and Char, K. . Polymer Nanotubules Obtained by Layer-by-Layer Deposition within AAO-Membrane Templates with Sub-100-nm Pore Diameters. *Small* **2010**, *6*, 2683-2689.

(11) Md Jani, A. M.; Losic, D.; Voelcker, N. H. Nanoporous anodic aluminium oxide: Advances in surface engineering and emerging applications. *Prog. Mater. Sci.* **2013**, *58*, 636-704.

(12) Tarish, S.; Wang, Z.; Al-Haddad, A.; Wang, C.; Ispas, A.; Romanus, H.; Schaaf, P.; Lei, Y. Synchronous Formation of ZnO/ZnS Core/Shell Nanotube Arrays with Removal of Template for Meliorating Photoelectronic Performance. *J. Phys. Chem. C* **2015**, *119*, 1575-1582.

(13) Rafailovic, L. D.; Gammer, C.; Rentenberger, C.; Trisovic, T.; Kleber, C.; Karnthaler, H. P. Functionalizing Aluminum Oxide by Ag Dendrite Deposition at the Anode during Simultaneous Electrochemical Oxidation of Al. *Adv. Mater.* **2015**, *27*, 6438–6443.

(14) Zeng, Z. Y.; Huang, X.; Yin, Z. Y.; Li, H.; Chen, Y.; Li, H.; Zhang, Q.; Ma, J.; Boey, F.; Zhang, H. Fabrication of Graphene Nanomesh by Using an Anodic Aluminum Oxide Membrane as a Template. *Adv. Mater.* **2012**, *24*, 4138-4142.

(15) Cheng, G.; Moskovits, M. A Highly Regular Two-Dimensional Array of Au Quantum Dots Deposited in a Periodically Nanoporous GaAs Epitaxial Layer. *Adv. Mater.* **2012**, *14*, 1567–1570.

(16) Liu, Y.; Bartal, G.; Zhang, X. All-angle negative refraction and imaging in a bulk medium made of metallic nanowires in the visible region. *Opt. Express* **2008**, *16*, 15439-15448.

(17) Fang, A.; Koschny, T.; Soukoulis, C. M. Optical anisotropic metamaterials: Negative refraction and focusing. *Phys. Rev. B* **2009**, *79*, 245127-245121- 245127-245127.

(18) Wang, H. J.; Zhou, W. H.; Yin, X. F.; Zhuang, Z. X.; Yang, H. H.; Wang, X. R. Template synthesized molecularly imprinted polymer nanotube membranes for chemical separations. *J. Am. Chem. Soc.* **2006**, *128*, 15954-15955.

(19) Kumeria, T.; Yu, J. X.; Alsawat, M.; Kurkuri, M. D.; Santos, A.; Abell, A. D.; Losic, D. Photoswitchable Membranes Based on Peptide-Modified Nanoporous Anodic Alumina: Toward Smart Membranes for On-Demand Molecular Transport. *Adv. Mater.* **2015**, *27*, 3019-3024.

(20) Wen, L.; Wang, Z.; Mi, Y.; Xu, R.; Yu, S. H.; Lei, Y. Designing Heterogeneous 1D Nanostructure Arrays Based on AAO Templates for Energy Applications. *Small* **2015**, *11*, 3408-3428.

(21) Moon, S.; Jung, Y. H.; Jung, W. K.; Jung, D. S.; Choi, J. W.; Kim, D. K. Encapsulated Monoclinic Sulfur for Stable Cycling of Li-S Rechargeable Batteries. *Adv. Mater.* **2013**, *25*, 6547-6553.

(22) Liu, J.; Wang, H. Q.; Chen, Z. P.; Moehwald, H.; Fiechter, S.; van de Krol, R.; Wen, L. P.; Jiang, L.; Antonietti, M. Microcontact-Printing-Assisted Access of Graphitic Carbon Nitride Films with Favorable Textures toward Photoelectrochemical Application. *Adv. Mater.* **2015**, *27*, 712-718.

(23) Mubeen, S.; Lee, J.; Singh, N.; Kramer, S.; Stucky, G. D.; Moskovits, M. An autonomous photosynthetic device in which all charge carriers derive from surface plasmons. *Nat. Nanotechnol.* **2013**, *8*, 247-251.

(24) Xuming, Z.; Yu Lim, C.; Ru-Shi, L.; Din Ping, T. Plasmonic photocatalysis. *Rep. Prog. Phys.* **2013**, *76*, 046401.

(25) Kim, H. J.; Lee, S. H.; Upadhye, A. A.; Ro, I.; Tejedor-Tejedor, M. I.; Anderson, M. A.; Kim, W. B.; Huber, G. W. Plasmon-Enhanced Photoelectrochemical Water Splitting with Size-Controllable Gold Nanodot Arrays. *ACS Nano* **2014**, *8*, 10756-10765.

(26) Santos, A.; Balderrama, V. S.; Alba, M.; Formentin, P.; Ferre-Borrull, J.; Pallares, J.; Marsal, L. F. Nanoporous Anodic Alumina Barcodes: Toward Smart Optical Biosensors. *Adv. Mater.* **2012**, *24*, 1050-1054.

(27) Schweikhard, V.; Grubisic, A.; Baker, T. A.; Thomann, I.; Nesbitt, D. J. Polarization-dependent scanning photoionization microscopy: ultrafast plasmon-mediated electron ejection dynamics in single Au nanorods. *ACS Nano* **2011**, *5*, 3724-3735.

(28) Huang, Z., Meng, G., Huang, Q., Chen, B., Zhu, C. and Zhang, Z. Large-area Ag nanorod array substrates for SERS: AAO template-assisted fabrication, functionalization, and application in detection PCBs. *J. Raman Spectrosc.* **2013**, *44*, 240-246.

(29) Lee, J.; Mubeen, S.; Ji, X.; Stucky, G. D.; Moskovits, M. Plasmonic Photoanodes for Solar Water Splitting with Visible Light. *Nano Lett.* **2012**, *12*, 5014-5019.

(30) Sun, K.; Meng, G.; Huang, Q.; Zhao, X.; Zhu, C.; Huang, Z.; Qian, Y.; Wang, X.; Hu, X. Gap-tunable Ag-nanorod arrays on alumina nanotip arrays as effective SERS substrates. *J. Mater. Chem. C* **2013**, *1*, 5015-5022.

(31) Tang, H.; Meng, G.; Li, Z.; Zhu, C.; Huang, Z.; Wang, Z.; Li, F. Hexagonally arranged arrays of urchin-like Ag hemispheres decorated with Ag nanoparticles for surface-enhanced Raman scattering substrates. *Nano Res.* **2015**, *8*, 2261-2270.

(32) Al-Haddad, A.; Zhan, Z. B.; Wang, C. L.; Tarish, S.; Vellacheria, R.; Lei, Y. Facile Transferring of Wafer-Scale Ultrathin Alumina Membranes onto Substrates for Nanostructure Patterning. *ACS Nano* **2015**, *9*, 8584-8591.

(33) Lyu, S.-H.; Lee, J.-S. Highly scalable resistive switching memory cells using pore-size-controlled nanoporous alumina templates. *J. Mater. Chem.* **2012**, *22*, 1852-1861.

(34) Geyer, N.; Huang, Z.; Fuhrmann, B.; Grimm, S.; Reiche, M.; Nguyen-Duc, T.-K.; de Boor, J.; Leipner, H. S.; Werner, P.; Gösele, U. Sub-20 nm Si/Ge Superlattice Nanowires by Metal-Assisted Etching. *Nano Lett.* **2009**, *9*, 3106-3110.

(35) Shoso, S.; Yasuhiko, M.; Hiroyuki, S.; Takayuki, T. Formation of Al Dot Hexagonal Array on Si Using Anodic Oxidation and Selective Etching. *Jpn. J. Appl. Phys.* **2002**, *41*, L340-L343.

(36) Wang, Y. D.; Zang, K. Y.; Chua, S. J. Nonlithographic nanopatterning through anodic aluminum oxide template and selective growth of highly ordered GaN nanostructures. *J. Appl. Phys.* **2006**, *100*, 054306-054301-054304.

(37) Wu, M., Wen, L., Lei, Y., Ostendorp, S., Chen, K. and Wilde, G. Ultrathin Alumina Membranes for Surface Nanopatterning in Fabricating Quantum-Sized Nanodots. *Small* **2010**, *6*, 695–699.

(38) Hideki, M.; Mitsutaka, N.; Takuya, M.; Kazuyuki, N. Long-Range-Ordered Anodic Porous Alumina with Reduced Hole Interval Formed in Highly Concentrated Sulfuric Acid Solution. *Jpn. J. Appl. Phys.* **2006**, *45*, L406.

(39) Malinovskis, U.; Poplausks, R.; Apsite, I.; Meija, R.; Prikulis, J.; Lombardi, F.; Erts, D. Ultrathin Anodic Aluminum Oxide Membranes for Production of Dense Sub-20 nm Nanoparticle Arrays. *J. Phys. Chem. C* **2014**, *118*, 8685-8690.

(40) https://www.fishersci.com/shop/products/falcon-cell-strainers-4/p-48680.

(41) Zhan, Z.; Lei, Y. Sub-100-nm Nanoparticle Arrays with Perfect Ordering and Tunable and Uniform Dimensions Fabricated by Combining Nanoimprinting with Ultrathin Alumina Membrane Technique. *ACS Nano* **2014**, *8*, 3862-3868.

(42) Han, C. Y.; Willing, G. A.; Xiao, Z.; Wang, H. H. Control of the Anodic Aluminum Oxide Barrier Layer Opening Process by Wet Chemical Etching. *Langmuir* **2007**, *23*, 1564-1568.

(43) Solanki, P. R.; Kaushik, A.; Agrawal, V. V.; Malhotra, B. D. Nanostructured metal oxide-based biosensors. *NPG Asia Mater.* **2011**, *3*, 17-24.

(44) Chen, J., Albella, P., Pirzadeh, Z., Alonso-González, P., Huth, F., Bonetti, S., Bonanni, V., Åkerman, J., Nogués, J., Vavassori, P., Dmitriev, A., Aizpurua, J. and Hillenbrand, R. . Plasmonic Nickel Nanoantennas. *Small* **2001**, *7*, 2341-2347.

(45) Atwater, H. A.; Polman, A. Plasmonics for improved photovoltaic devices. *Nat. Mater.* **2010**, *9*, 205-213.

(46) Green, M. A.; Pillai, S. Harnessing plasmonics for solar cells. *Nat. Photonics* **2012**, *6*, 130-132.

(47) Hägglund, C.; Apell, S. P. Plasmonic Near-Field Absorbers for Ultrathin Solar Cells. *J. Phys. Chem. Lett.* **2012**, *3*, 1275-1285.

(48) Linic, S.; Christopher, P.; Ingram, D. B. Plasmonic-metal nanostructures for efficient conversion of solar to chemical energy. *Nat. Mater.* **2011**, *10*, 911-921.

(49) Thomann, I.; Pinaud, B. A.; Chen, Z.; Clemens, B. M.; Jaramillo, T. F.; Brongersma, M. L. Plasmon Enhanced Solar-to-Fuel Energy Conversion. *Nano Lett.* **2011**, *11*, 3440-3446.

(50) Li, J.; Cushing, S. K.; Zheng, P.; Meng, F.; Chu, D.; Wu, N. Plasmon-induced photonic and energy-transfer enhancement of solar water splitting by a hematite nanorod array. *Nat. Commun.* **2013**, *4*.

(51) Liu, Z.; Hou, W.; Pavaskar, P.; Aykol, M.; Cronin, S. B. Plasmon Resonant Enhancement of Photocatalytic Water Splitting Under Visible Illumination. *Nano Lett.* **2011**, *11*, 1111-1116.

(52) Kale, M. J.; Avanesian, T.; Christopher, P. Direct Photocatalysis by Plasmonic Nanostructures. *ACS Catal.* **2014**, *4*, 116-128.

(53) Kim, S. J.; Thomann, I.; Park, J.; Kang, J. H.; Vasudev, A. P.; Brongersma, M. L. Light trapping for solar fuel generation with Mie resonances. *Nano Lett.* **2014**, *14*, 1446-1452.

(54) Clavero, C. Plasmon-induced hot-electron generation at nanoparticle/metal-oxide interfaces for photovoltaic and photocatalytic devices. *Nat. Photonics* **2014**, *8*, 95-103.

(55) Brongersma, M. L.; Halas, N. J.; Nordlander, P. Plasmon-induced hot carrier science and technology. *Nat. Nanotechnol.* **2015**, *10*, 25-34.

(56) Robatjazi, H.; Bahauddin, S. M.; Doiron, C.; Thomann, I. Direct Plasmon-Driven Photoelectrocatalysis. *Nano Lett.* **2015**, *15*, 6155-6161.

(57) Hägglund, C.; Zeltzer, G.; Ruiz, R.; Thomann, I.; Lee, H.-B.-R.; Brongersma, M. L.; Bent, S. F. Self-Assembly Based Plasmonic Arrays Tuned by Atomic Layer Deposition for Extreme Visible Light Absorption. *Nano Lett.* **2013**, *13*, 3352-3357.

(58) Chen, W.; Wu, Y.; Yue, Y.; Liu, J.; Zhang, W.; Yang, X.; Chen, H.; Bi, E.; Ashraful, I.; Gratzel, M.; Han, L. Efficient and stable large-area perovskite solar cells with inorganic charge extraction layers. *Science* **2015**, *350*, 944-948.

(59) Nilsson, P. O.; Norris, C.; Walldén, L. The electronic structure of gold studied by photoemission. *Phys. Kondens. Mater.* **1970**, *11*, 220-230.

Table of Contents/Abstract Graphics